SCIENTIFIC REPORTS

OPEN

SUBJECT AREAS:
ELECTRONIC PROPERTIES AND MATERIALS
SURFACES, INTERFACES AND THIN FILMS
MOLECULAR SELF-ASSEMBLY
IMAGING TECHNIQUES

Received
30 October 2012

Accepted
21 February 2013

Published
18 March 2013

Correspondence and requests for materials should be addressed to F.K. (florian.klappenberger@tum.de) or J.V.B. (jvb@ph.tum.de)

Assessment of Scanning Tunneling Spectroscopy Modes Inspecting Electron Confinement in Surface-Confined Supramolecular Networks

Wolfgang Krenner, Dirk Kühne, Florian Klappenberger & Johannes V. Barth

Physik Department E20, Technische Universität München, James-Franck Straße, 85748 Garching, Germany.

Scanning tunneling spectroscopy (STS) enables the local, energy-resolved investigation of a samples surface density of states (DOS) by measuring the differential conductance (dI/dV) being approximately proportional to the DOS. It is popular to examine the electronic structure of elementary samples by acquiring dI/dV maps under constant current conditions. Here we demonstrate the intricacy of STS mapping of samples exhibiting a strong corrugation originating from electronic density and local work function changes. The confinement of the Ag(111) surface state by a porous organic network is studied with maps obtained under constant-current (CC) as well as open-feedback-loop (OFL) conditions. We show how the CC maps deviate markedly from the physically more meaningful OFL maps. By applying a renormalization procedure to the OFL data we can mimic the spurious effects of the CC mode and thereby rationalize the physical effects evoking the artefacts in the CC maps.

Shortly after the initial demonstration of scanning tunneling microscopy (STM)[1], theoretical analysis of electron tunneling through the vacuum barrier has shown that the tunneling current I_T depends on the local density of states (LDOS) of the sample[2,3]. Subsequently, scanning tunneling spectroscopy (STS) was introduced, providing access to the energy dependence of the LDOS[4,5] and enabling the local characterization of physical and chemical properties of conducting samples. The powerful capabilities of STM/STS have been demonstrated in the investigation of the local electronic properties of surfaces[6–11]. The key advantage of STS over the classical, spatially averaging spectroscopy techniques is its capability to investigate the electronic structure on the atomic scale, while at the same time providing topographic information. Therefore, STS is perfectly suited to study adsorbates positioned on substrates[12–15] and confinement effects of surface state electrons[16–24], providing a complementary approach to k-vector resolving photoemission spectroscopy techniques[24–26].

STS is typically carried out by measuring the differential conductance (dI/dV) under open feedback-loop (OFL) conditions by applying to the bias voltage V_B a small harmonic modulation with a specific frequency ω_{mod} and extracting the corresponding modulation-related signal via a lock-in technique. Within certain approximations[27,28], the recorded dI/dV signal is proportional to the LDOS $\rho_S(\vec{r},E)$ of the sample at the position of the STM tip $\vec{r}$ and energy E. When focusing on the spatial distribution of the LDOS of a specific area (x, y), spectroscopy data is often acquired by recording dI/dV while simultaneously scanning the tip with a constant I_T in order to obtain contour maps for a certain energy $E_B = eV_B$. However, as was already demonstrated earlier[29–36], in this so-called constant-current (CC) mode, the dI/dV signal does not only depend on the DOS, but is convoluted with the change in tip-sample separation z. This convolution results from the dependence of I_T and dI/dV on the transmission probability T as can be seen when expressing the quantities within the 1D-WKB approximation[7,27,36,37]. Since T depends exponentially on z both quantities change drastically upon variation of z. In simple systems meaningful LDOS information can be retrieved from the convoluted CC data by estimating the change of T from the z-signal[36,38]. However, when complex systems with appreciable surface corrugation and local variation of the work function are under investigation, T depends non-trivially on z and this method fails.

In this work we first shortly assess the theoretical background for space-resolved dI/dV measurements of inhomogeneous samples. Then, we discuss the effect of a varying tip-sample separation during a two-dimensional (2D) measurement on the experimental spectroscopy data of molecular networks confining the quasi-free 2D electron gas of the Ag(111) surface state to periodic quantum dot arrays[22,23].

By comparing datasets of 2D dI/dV maps acquired in both CC and OFL mode, we directly relate the different measurement techniques and exemplify the strong deviations of the CC maps from the physically straightforward OFL counterparts. We thus demonstrate that the CC data can be misleading even on a qualitative level for the investigated corrugated systems. Finally, we introduce a special renormalization procedure, accounting for the locally changing T which allows us to reproduce the CC maps from the OFL dataset. The successful reproduction is consistent with the theoretic understanding of the spectroscopy modes.

Results

Theoretical considerations. In a first step, we review the dependence of the STS signal on the transmission probability and the density of states $\rho_S(E)$ between the Fermi energy $E_F = 0$ of the sample and the energy $E_B = eV_B$ at which the dI/dV signal is measured. In the WKB approximation for planar electrodes[6] I_T depends on the DOS of the tip, ρ_T, the DOS of the sample, ρ_S, and on the transmission probability T:

$$I_T \propto \int_0^{eV_B} \rho_T(eV-E)\rho_S(\vec{r}_T,E)T(z,eV,E)\mathrm{d}E \qquad (1)$$

In this description, the transmission probability for electrons with energy E to tunnel across the vacuum barrier is given by

$$T(z,eV,E) = \exp\left(-z(\vec{r})\sqrt{\frac{4m}{\hbar^2}(\Phi_T+\Phi_S+eV-2E)}\right) \qquad (2)$$

with the tip-sample separation $z(\vec{r})$ at the lateral position $\vec{r}=(x,y)$, the effective electron mass m, and the work functions of the tip and the sample materials, Φ_T and Φ_S respectively.

Even when ρ_T is assumed to be constant, the dI/dV signal is no longer directly proportional to ρ_S when T changes perpetually while dI/dV is measured in CC mode:

$$\left.\frac{\mathrm{d}I}{\mathrm{d}V}\right|_{V_B} \propto \rho_S(eV)T(z,eV) + \int_0^{eV_B} \rho_S(E)\frac{\partial T(eV,E)}{\partial V}\mathrm{d}E \qquad (3)$$

In this expression, the second term accounts for high energy contributions which we neglect in this consideration. Instead, we concentrate on the influence of ρ_S and T to account directly for the experimental conditions when acquiring dI/dV maps in CC mode at low bias. For calculations we therefore use the expression

$$\left.\frac{\mathrm{d}I}{\mathrm{d}V}\right|_{V_B} \propto \rho_S(eV_B)T(z,eV_B) \qquad (4)$$

for the differential conductance.

Origin of artefacts in the spectroscopic data recorded in the CC mode. To illustrate the difference between dI/dV measurements in OFL and CC mode, we first discuss three exemplary cases of E- and x-dependencies (gray, blue, and red in Fig. 1) in a simple model system, namely a topographically featureless, flat surface, divided into two regions I and II being traversed during the measurement. Assuming a W tip over the Ag(111) surface, the work functions were chosen as $\Phi_T = 4.55$ eV and $\Phi_S = 4.74$ eV and $m = 0.42$ m$_e$ was set for the Ag(111) surface state electrons[25,39]. Without loss of generality we focus on the energy range from $E_F = 0$ eV to $E_1 = 0.1$ eV.

In the first example (gray with squares in Fig. 1), we consider two different energy dependencies of $\rho_S(E, x)$ in the two regions I and II (Figs. 1a and b) resulting in the same state density at the energy of interest E_1, namely $\rho_S(E, x < 1)$ increases from 0 for $E = 0$ to 1.5 for $E = E_1$ and $\rho_S(E, x > 1)$ decreases from 3 to 1.5 in the same range. Thus, at $E = E_1$ the state density is the same in both regions and accordingly the measurement of $\rho_S(E_1)$ along x should give a region independent

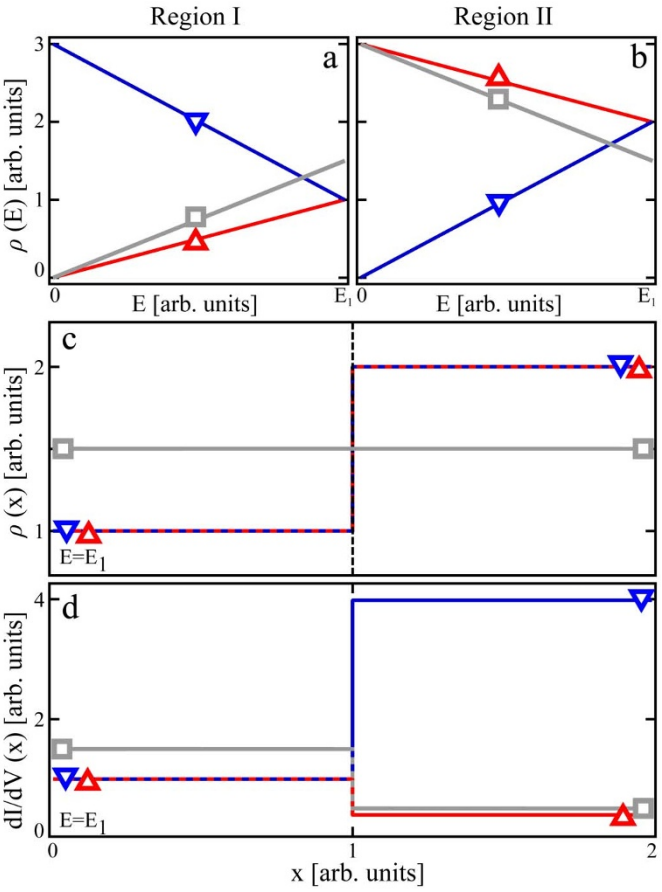

Figure 1 | Model system and simulated dI/dV traces. (a) and (b) Different energy dependencies for the local density of states $\rho_S(E)$ are assumed in regions I and II. (c) For the two regions different spatial distributions for $\rho_S(x, E_1)$ at energy E_1 represent the reference quantities that are to be reproduced. (d) Simulated dI/dV traces along x obtained in CC mode. The simulated traces deviate strongly from the reference signals in (c). In the red (upward-pointing triangles) and gray (squares) scenario, the $\rho_S(x)$ features are not reproduced correctly, in the blue case (downward-pointing triangles) the step is reproduced only qualitatively.

constant signal (Fig. 1c). However, the calculated CC mode dI/dV signal (Fig. 1d) exhibits a step. The CC signal was simulated by first finding z and T by self-consistently solving Eq. (1) and (2) for identical I_T in both regions and then calculating the dI/dV signals in both regions via Eq. (4). The CC mode dI/dV signal is smaller in region II because the integrated density of states between $E = 0$ and $E = E_1$ is larger in region II causing a retraction of the tip for establishing the constant I_T and thereby a reduction of T.

In a second and third example (red with upward-pointing triangles and blue with downward-pointing triangles in Fig. 1) we consider an identical step-wise increase in $\rho_S(x, E_1)$ when moving the tip from region I to region II (Fig. 1c), combined with different linear energy dependencies of $\rho_S(x, E)$ in the two regions (Fig. 1a and b, red and blue). The calculated dI/dV signal (Fig. 1d) exhibits an exaggerated step (factor 2) in the blue case and an inverted step in the red case.

These examples demonstrate the strong impact of T on the dI/dV signal obtained in the CC mode where the tip-sample separation is perpetually adjusted to maintain a constant I_T. Thus, the spatial dependence of a dI/dV signal recorded at an energy E_1 in CC mode can only in special cases be associated with the actual spatial dependence of the sample LDOS at that energy. In general, such measurements suffer from incorrect intensity ratios and yield even

qualitatively wrong behavior when comparing spectral densities at different positions.

The artifacts in the dI/dV signal resulting from a spatially non-constant T can not only result from changes in the tip-sample gap distance z as discussed so far, but also from local variations of the sample work function Φ_S, even when the tip is scanned at a constant height. Therefore, we address the effects of local Φ_S variations on dI/dV measurements in CC mode. To this end we assume a flat, featureless surface with constant $\rho_S(x, E)$ and with two regions, one having a low work function $\phi_{S,1} = 3.74$ eV and one having a $\Phi_{S,2} = 4.74$ eV. When we calculate the CC-dI/dV signals, the deviation in both regions is quite low. Even though a reduced work function results in a higher tip-sample separation, the integrated transmission probability $\int_0^{eV} T\mathrm{d}E$ is identical (cf. Fig. 2). However, the difference for the absolute values of T at the setpoint (here: $I_T = 0.1$ nA, $E_B = 0.2$ eV) is notable (1.5%). Thus, care has to be taken, when dI/dV spectra are measured on a system with variable Φ_S.

Imaging a porous molecular network. In order to obtain a physically meaningful comparison of spectral intensities at different positions on the sample, we use the following procedure which should in principle be applicable to any other system. It is important to carefully select a proper setpoint for stabilizing the tip before recording the OFL spectra. In our case of the confined surface state on Ag(111) we choose $E_B = -0.2$ eV and $I_T = 0.1$ nA. At this energy the contributions of the molecular orbitals are small and the surface state-related DOS is not present, i.e., the sample DOS originates from the projected bulk DOS of Ag only. Accordingly, the dI/dV signal is to a good approximation constant in the whole area (x,y) of interest. It follows that the artifacts produced by local tunneling gap changes originating from local work function changes can be eliminated by normalizing all spectra such that they have the same dI/dV value at the setpoint energy, see Eq. (4). This is, because under such tunneling conditions, the tip in CC mode follows a contour of constant $\int_0^{eV} T\mathrm{d}E$, which can be compensated for, in a first approximation, by the mentioned normalization condition. In our case, where the dI/dV is featureless in the energy range between -0.2 V and -0.1 V, the arithmetic mean value m_i of all the bias points within this energy interval of the dI/dV was calculated for each spectrum i. Subsequently, each spectrum was multiplied by a normalization factor $f_i = f/m_i$, where f is in principle a deliberate value, but typically the mean value of all m_i is used. This allows us to directly compare spectral intensities within the pores and on the molecules in a unified framework. A further normalization via the division by the measured I/V, which is typically performed for semiconducting surfaces[7,40], was not performed due to the approximately linear I/V encountered on the metal surface in the energy interval of interest.

In order to understand and qualitatively assess the challenges addressed above, we study the effects of CC mode dI/dV measurements in the model system of Ag(111) 2D surface state electrons that are confined to 0D quantum wells via organic molecular networks self-assembled from sexiphenyl dicarbonitrile (for structure model, see Fig. 3)[41]. The confining properties and resulting bound states were described experimentally and assessed via Boundary Element Method simulations in previous studies[22,23].

The exact contrast mechanisms for molecules being imaged in STM is currently still widely discussed[42–47]. Molecules often markedly

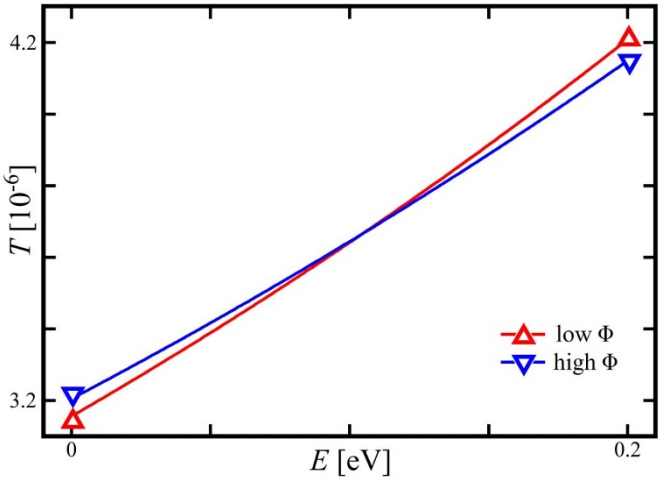

Figure 2 | Calculated T in two otherwise featureless sample regions with different work functions Φ. Whereas the integrated transmission probability which contributes to I_T is identical in both cases (low Φ displayed in red with upward-pointing triangles, high Φ in blue with downward-pointing triangles), the absolute values differ notably (1.5%) at the selected setpoint ($I_T = 0.1$ nA, $E_B = 0.2$ eV).

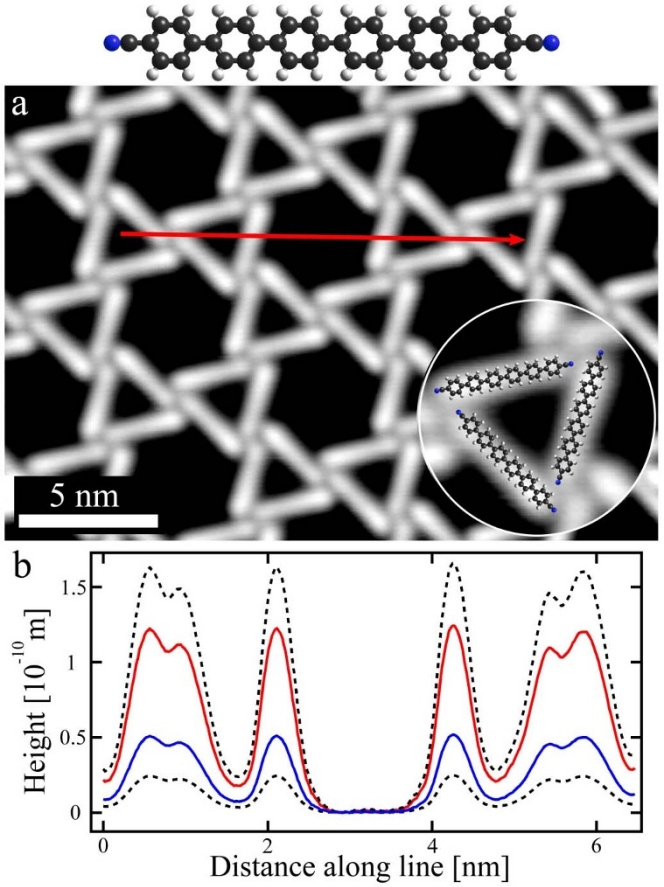

Figure 3 | Imaging parameter dependent appearance of an organic network. Top: structure model of sexiphenyl dicarbonitrile (C black, N blue, H white). (a) One possible network among the different self-assembled, organic phases is the kagomé lattice. The open-porous network follows a four-fold bonding motif and each molecule interacts with five adjacent molecules (inset). $I_T = 0.1$ nA, $V_B = -0.5$ V (b) Height profile extracted along the red line in (a) shows that the apparent molecule height at these tunneling parameters is ~ 1.2 Å (red profile). Depending on the tip and tunneling parameters, the molecule height varied between 0.2 Å and 1.6 Å (black dashed lines display upper and lower limit). The blue profile shows the calculated tip-sample separation when a local lowering of the electron work function by 1 eV at the position of the molecules is assumed at $I_T = 0.1$ nA and $V_B = 0.2$ V.

appear in STM topographs at bias voltages in the gap between the lowest unoccupied and highest occupied molecular orbitals where the orbital-related contributions to the tunnel current should be irrelevant. Therefore different effects are necessary to explain this phenomenon. Among others, a local variation of the work function is a possible candidate to rationalize molecule imaging. In the case of self-assembled, organic sexiphenyl dicarbonitrile networks in which the molecules appear as stick-like protrusions and the network bonding follows a four-fold nodal motif, one of the possible geometries is the kagomé network (see Fig. 3a). When a topographical line-scan across the molecule network is extracted along the red line in Fig. 3a, the apparent height of the molecules varies depending on the experimental conditions in the interval of ~0.2–1.6 Å. In Fig. 3b the actual line scan (red, obtained at $V_B = -0.5$ V) is displayed along with the upper and lower limit of the observed height (dashed, black lines). From STS we know that the LUMO of these molecules is positioned at around $V_B = 1.5$ V. Taking into account that for polyphenylene molecules the HOMO-LUMO gap is typically more than 3 eV, the line scan was recorded near to the center of the HOMO-LUMO gap suggesting that the contribution of the frontier orbitals to the molecular contrast is very weak. The deposition of sexiphenyl molecules onto the Au(111) surface at monolayer coverage results in a lowering of the electron work function by 0.73 eV[48]. In the model system presented above a local reduction of Φ_S by 1 eV at constant ρ_S results in the tip being retracted by ~0.5 Å. This is in in the same ballpark as the apparent molecule height of ~0.2–1.6 Å in CC topographs and supports our reasoning that a significant molecular corrugation can be explained solely by work function considerations.

Comparing spectroscopic information obtained in OFL mode vs CC mode. When Ag(111) surface state electrons are confined within the molecular network, a set of localized electron states evolves. We first probe the system via OFL point spectroscopy (see Fig. 4). When we investigate specific positions within the network pores (Fig. 4a), we can identify the corresponding LDOS signatures (Fig. 4b, spectra in the quasi-hexagonal pore are offset from the spectra in the

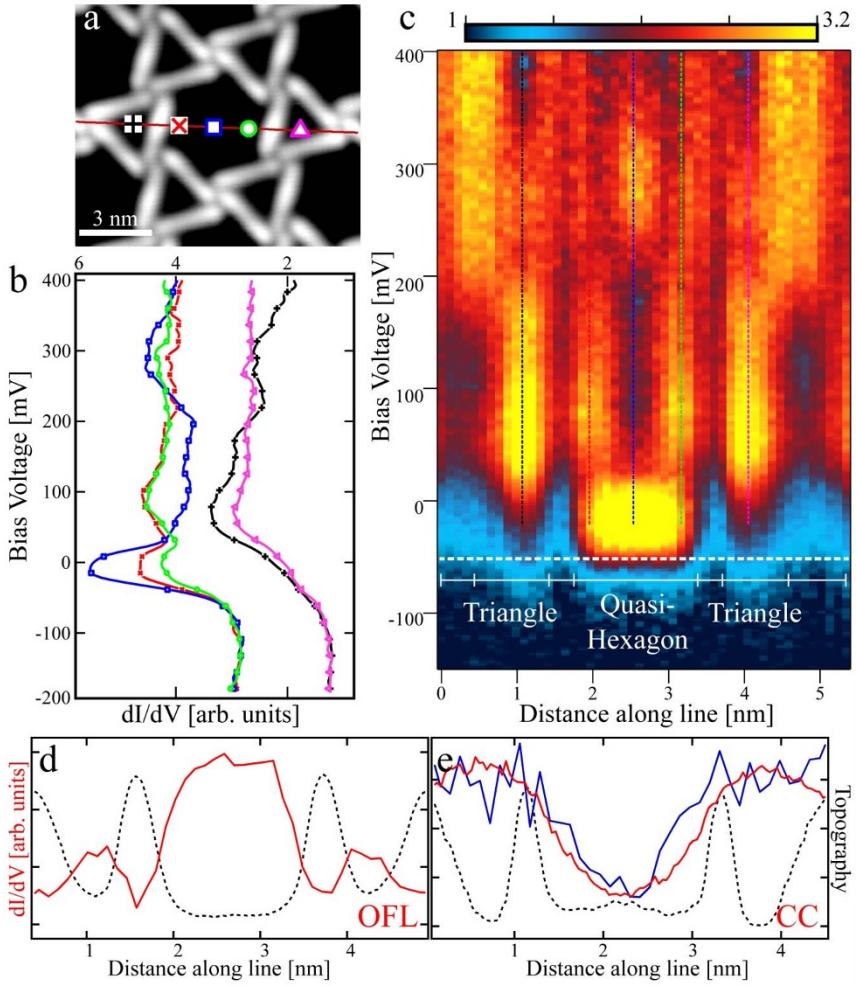

Figure 4 | OFL d*I*/d*V* spectra for a self-assembled supramolecular kagomé network on Ag(111). (a) In the topograph the positions of OFL point spectra are indicated. Colored symbols mark individual spectra displayed in (b) and the red line defines the positions of a total of 50 spectra visualized in (c). (b) At selected positions in the pores of the networks, different d*I*/d*V* fingerprints are identified (spectra in the two pore types are offset for clarity). (c) Color plot of 50 OFL spectra taken along the line indicated in (a) revealing a strong spatial variation of the LDOS within the network cavities. The expression of quantum confinement leading to defined electronic states becomes clear. The selected positions reproduced in (a and b) are indicated by respectively colored dashed lines. (d) A d*I*/d*V* profile (red solid line) extracted at −50 mV from the set of OFL spectra (displayed in (c) with the white dashed line) clearly shows the onset of the surface state in both pore types. On top of the molecules (represented by the peaks of the topographic line drawn with the black dashed line) the surface state is suppressed, i.e., low d*I*/d*V* intensity is found in agreement with their scattering properties. (e) In CC mode a higher, nearly constant spectral signal (red solid line) is observed across the smaller, triangular pores and molecules, whereas the quasi-hexagonal pore in the center shows a minimum. Upon renormalization in the energy interval [–50 mV…0 mV] the OFL data (blue solid line) reproduces the observations of the CC mode (related topography profile indicated by a black dashed line).

triangular pores for clarity). In the center of the quasi-hexagonal pore (blue) two features are observed at −5 mV and 280 mV, respectively. Towards the cavity rim (red and green) the intensity of the peaks at −5 mV and 280 mV decreases, however an intermediate feature at 80 mV is found. In the smaller triangular pores (black and magenta) the first state is shifted towards higher energies (70 mV) due to the reduced quantum dot size.

When all 50 spectra acquired along a line across the different pores (Fig. 4a, red line) are depicted in a color plot (Fig. 4c, respectively colored dashed lines indicate positions of point spectra displayed in Fig. 4a), the spatial and energetic variation of the LDOS becomes even more clear. In the central cavity the states featuring 0, 1 and 2 nodes can be identified. The triangular pores show an energetically broader intensity maximum, with the expression of individual states being less clear. A deeper analysis of the system was presented in Ref. 22.

The kagomé model system will now serve for a comparison of the CC and OFL spectroscopy techniques. In a first step, we compare dI/dV signals acquired across the open pores of the self-assembled network, see Fig. 4a. At $E_B = -50$ mV the dI/dV intensity extracted from the 50 OFL point spectra presented above (Fig. 4d) is related to measurements performed in CC mode (Fig. 4e, red). Distinctively different dI/dV distributions are measured in both operation modes.

The OFL technique leads to maxima at the center of the pores, whereas on top of the molecules minima are found (Fig. 4d, red). In contrast, dI/dV measurements at identical energy in CC mode contradict this finding (Fig. 4e, red). Here, the central pore shows a depression, whereas the molecules and smaller cavities show approximately constant dI/dV at higher intensity. Thus the LDOS variation obtained in CC mode fails to qualitatively reproduce the behavior expected for confined electrons in the network cavities in this strongly corrugated system, even relatively close to E_F. However, the influence of T on the CC mode can be reproduced by employing the normalization procedure presented earlier in the energy interval from E_F to E_B to the OFL dataset instead of the spectroscopically featureless setpoint region, yielding the blue curve in Fig. 4e. Via this renormalization the dI/dV signature observed in CC mode is qualitatively reproduced by the renormalized OFL dataset.

When we extend the comparison of CC and OFL dI/dV measurements towards 2D mapping of the LDOS, the strikingly different observations for both modes in the line-scan are further elucidated. We directly relate maps acquired in OFL and CC mode at −50 mV and 250 mV in Fig. 5. The OFL dI/dV maps were extracted from point spectra on a 84 × 84 pixel grid equally distributed over the area displayed in the topographic image in Fig. 5a, where for each spectrum the tip was stabilized at $E_B = -200$ mV and $I_T = 0.1$ nA. Figures 5b and e represent the OFL maps for $E_B = -50$ mV and 250 mV respectively and are given with the identical color code as in Fig. 4c. In comparison, CC dI/dV maps are shown in Fig. 5c and f.

The −50 mV OFL map (Fig. 5b) is in accordance with the line of spectra shown in Fig. 4. As expected, we observe the onset of the first bound state within the triangular and the quasi-hexagonal pores, whereby the molecules show the lowest intensity. The CC dI/dV map at the same bias voltage (Fig. 5c) shows increased spectral density above the molecular backbones and triangular pores, whereas the quasi-hexagonal pores show low intensity. Note that the CC map was recorded over a domain exhibiting the opposite chiral enantiomorph of the network which is barely visible in the features of the network, but explains the different positions of the centers of the pores. From our earlier work[22] we know that the chirality signature does not influence the other properties of the confined electron states. When the OFL dataset is renormalized in an identical fashion as in Fig. 4e, the dI/dV map changes drastically. The renormalized OFL map (Fig. 5d) now closely resembles the data acquired in CC mode. The maximum intensity is also found on the molecules and triangular pores, whereas the quasi-hexagonal pores show depressions. Thus,

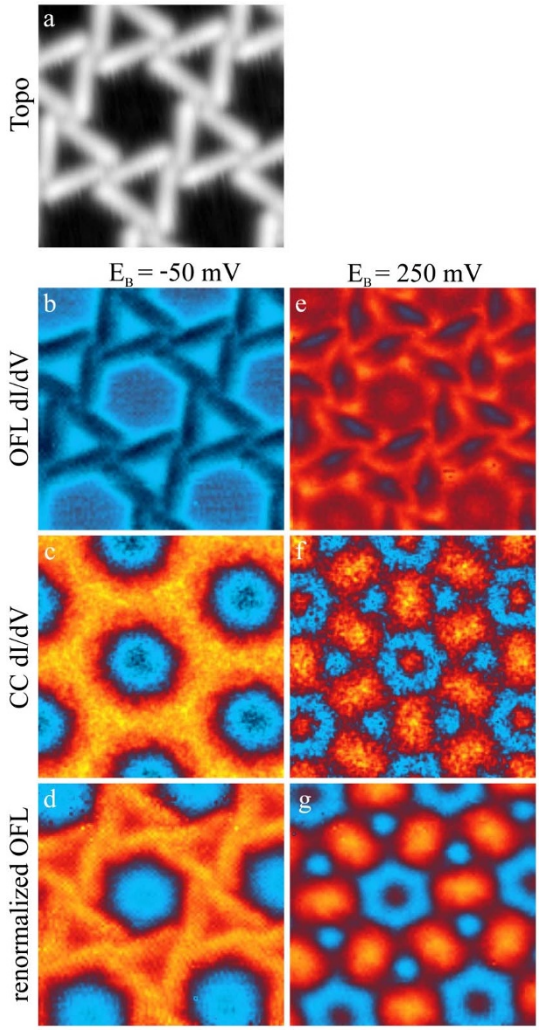

Figure 5 | Comparison of 2D dI/dV maps acquired in CC and OFL mode. (a) Topograph image of the area over which the OFL spectra were distributed ($I_T = 0.1$ nA and $V_B = -0.2$ V). (b)–(d) $E_B = -50$ mV: (b) The dI/dV map obtained in OFL mode displays the onset of the first confined state in the triangular and quasi-hexagonal pore, respectively. (c) The map acquired in CC mode shows higher intensity over the molecular ligands and triangular pores, whereas the quasi-hexagonal pores feature depressions. (d) After renormalization of the OFL map over the energy range $E_F \rightarrow E_B$, the observations found in CC mode are reproduced qualitatively. (e)–(g) $E_B = 250$ mV: (e) The OFL map shows confined states in both pores alongside depressions at the positions of the molecules. (f) The CC map exhibits high intensity on the binding motifs and in the center of the quasi-hexagonal pores. Thus the spatial dependence of $\rho_S(E_B)$ is obtained in an even qualitatively wrong manner. (g) The renormalized OFL map reproduces the CC map in great detail. Relative intensities and spatial distributions of the observed features show good agreement. The color-code of all maps is identical to that used for Fig. 4c.

a good agreement between the CC dI/dV map and the renormalized OFL map is achieved.

Further away from E_F, at $E_B = 250$ mV, the OFL dI/dV map shows different confined states in both pores (Fig. 5e). In the quasi-hexagonal pore, maxima are found in the center and close to the corners. The triangular pores exhibit a density distribution that resembles a three winged propeller. In comparison, the CC dI/dV map again differs markedly from the expected distribution of confined electron states (Fig. 5f). The maximum intensity is now found on the binding motifs of the molecular network, leading to six rectangular features surrounding the quasi-hexagonal pore. In the center

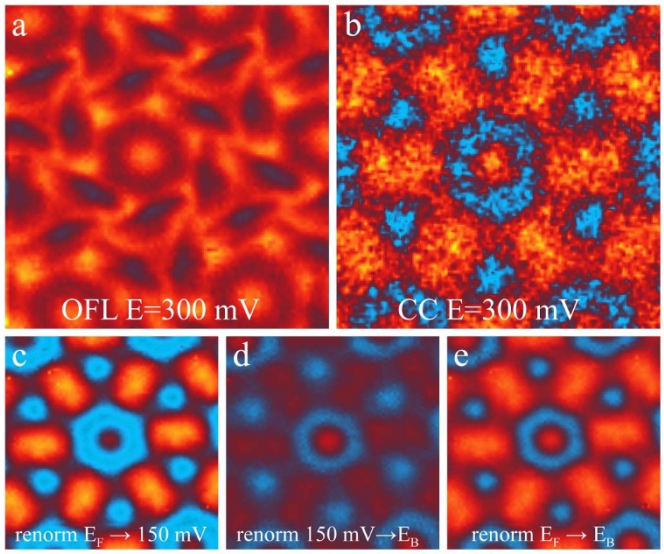

Figure 6 | Effect of partial renormalization intervals. (a) OFL map acquired at $E_B = 300$ mV. (b) CC map acquired at $E_B = 300$ mV. When the OFL map is renormalized only over either half of the entire energy interval ($E_F \rightarrow 150$ mV in (c) and 150 mV $\rightarrow 300$ mV in (d)) the relative intensities of the different features and and their related spatial distribution are only poorly reproduced. (e) When the OFL data are renormalized in the energy interval $E_F \rightarrow E_B$ the obtained map agrees quantitatively with (b).

we observe a maximum, surrounded by a hexagonal depression. In contrast, the triangular pores feature minimal intensity. Therefore, in CC mode merely the maximum in the center of the large pore is reproduced. After the OFL map was renormalized with the normalization interval ranging from E_F to 250 mV, the map nicely matches that acquired in CC mode. The overall spatial distribution as well as the relative intensity of the observed features agree well.

Discussion

The analysis presented exemplifies that by renormalizing the OFL dI/dV maps, the data from CC dI/dV maps can be reproduced in great detail (see the Supporting Information for an extended series of dI/dV maps). This effect can be attributed to the operation of the feedback loop in CC mode. When I_T is kept constant for a given bias voltage, the tip-sample separation z is perpetually adjusted to compensate for changes in ρ_S during the scan. Therefore, by maintaining a constant I_T, the feedback loop operation entails an integration over the LDOS between E_F and E_B to account for the spatial changes in tunneling probability. By employing the renormalization procedure, this effect is reproduced mathematically from the OFL spectra. When all spectra are subsequently renormalized to their mean dI/dV value in the interval $E_F \rightarrow E_B$, the LDOS contribution to the tunneling current and thereby the readjustment of T at every position is simulated. The relative intensities of all spectra are shifted depending on the ratio between the mean spectral intensity and the actual intensity. Thereby, the effect of a variable tip-sample separation and finally the dI/dV maps acquired in CC mode are reproduced.

Finally we demonstrate that all states in the range between E_F and E_B contribute to the artifacts obtained in CC mode. In Fig. 6b, a CC dI/dV map acquired at $E_B = 300$ mV is shown alongside the renormalized ($E_F \rightarrow E_B$) OFL map in Fig. 6e. At this energy, the rectangular features located on the binding motifs and the maximum in the center of the quasi-hexagonal pore exhibit an identical intensity in the CC dI/dV map and the renormalized OFL map. When the OFL map is renormalized over the energy ranges $E_F \rightarrow 150$ mV and 150 mV $\rightarrow E_B$ (see Fig. 6c and d), respectively, the maps are already similar to the CC map. However, the relative intensities are qualitatively wrong. In Fig. 6c the rectangular units show higher intensity than the maximum in the center of the quasi-hexagonal pore. Furthermore, the peak in the center has a smaller diameter than in the CC dI/dV map. Contrarily, in Fig. 6d the central maximum is spatially more extended with higher intensity than the rectangular units on the binding motifs. Thus, only the renormalization over the entire energy range can reproduce the findings from CC dI/dV mapping in detail.

In summary, we conducted a detailed STS investigation of the surface state confinement in a nano-porous organic network focusing on the comparison of spectroscopic data recorded in both constant-current and open-feedback-loop mode of the very same system. The spurious effects of the variable tip-sample separation during CC measurements on highly corrugated samples with lateral work function variations were reported and analyzed. Our findings demonstrate and explain pitfalls that frequently occur in this method and thereby elucidate the intricacy of mapping the LDOS in two dimensions with STS. Especially for inhomogeneous systems great care has to be taken experimentally and during data processing. While CC dI/dV mapping is a viable tool to explore spatial distribution of electronic states in simple samples, physically meaningful LDOS maps of inhomogeneous systems can only be obtained when OFL spectroscopy is employed. Albeit acquiring datasets of OFL spectra on a grid is time consuming and experimentally challenging, it delivers a complete analysis of the energy range under investigation as opposed to recording individual CC maps. On the basis of a well-defined setpoint, OFL datasets enable a physically meaningful comparison of spectral intensities at different energies and positions. It is suggested that such considerations are generally relevant for the detailed understanding of electronic properties in organic-inorganic hybrid systems.

Methods

Scanning tunneling microscopy/spectroscopy. STM measurements were performed using a home-built LT-STM[49,50] in UHV ($3 \cdot 10^{-11}$ mbar base pressure) at temperatures below 10 K. The Ag(111) surface was prepared by repeated cycles of Ar^+ sputtering (flux$\approx 7 \frac{\mu A}{cm^2}$) and annealing to 740 K, in order to obtain atomically flat terraces separated by monatomic steps. Sexiphenyl dicarbonitrile molecules (for structure model, see Fig. 3) were deposited from a quartz crucible in an organic molecular beam epitaxy (OMBE) source at 585 K, while the substrate was held at room temperature. All topography was acquired at constant tunneling current with closed feedback loop. dI/dV signals were recorded with bias modulation at ~1400 Hz at a modulation amplitude of 5 mV rms, while the lock-in time constant was set to either 20 or 50 ms.

1. Binnig, G., Rohrer, H., Gerber, C. & Weibel, E. Surface studies by scanning tunneling microscopy. *Phys. Rev. Lett.* **49**, 57–61 (1982).
2. Tersoff, J. & Hamann, D. R. Theory and application for the scanning tunneling microscope. *Phys. Rev. Lett.* **50**, 1998–2001 (1983).
3. Lang, N. D. Vacuum tunneling current from an adsorbed atom. *Phys. Rev. Lett.* **55**, 230–233 (1985).
4. Binnig, G. *et al.* Tunneling spectroscopy and inverse photoemission: Image and field states. *Phys. Rev. Lett.* **55**, 991–994 (1985).
5. Becker, R. S., Golovchenko, J. A., Hamann, D. R. & Swartzentruber, B. S. Real-space observation of surface states on Si(111) 7 × 7 with the tunneling microscope. *Phys. Rev. Lett.* **55**, 2032–2034 (1985).
6. Hamers, R. J. Atomic-resolution surface spectroscopy with the scanning tunneling microscope. *Annu. Rev. Phys. Chem.* **40**, 531–559 (1989).
7. Feenstra, R. M. Scanning tunneling spectroscopy. *Surf. Sci.* **299–300**, 965–979 (1994).
8. Bürgi, L., Jeandupeux, O., Brune, H. & Kern, K. Probing hot-electron dynamics at surfaces with a cold scanning tunneling microscope. *Phys. Rev. Lett.* **82**, 4516–4519 (1999).
9. Morgenstern, K., Braun, K.-F. & Rieder, K.-H. Surface-state depopulation on small Ag(111) terraces. *Phys. Rev. Lett.* **89**, 226801 (2002).
10. McElroy, K. *et al.* Relating atomic-scale electronic phenomena to wave-like quasiparticle states in superconducting $Bi_2Sr_2CaCu_2O_{8+\delta}$. *Nature* **422**, 592–596 (2003).
11. Fischer, Ø., Kugler, M., Maggio-Aprile, I., Berthod, C. & Renner, C. Scanning tunneling spectroscopy of high-temperature superconductors. *Rev. Mod. Phys.* **79**, 353–419 (2007).
12. Stipe, B. C., Rezaei, M. A. & Ho, W. Single-molecule vibrational spectroscopy and microscopy. *Science* **280**, 1732–1735 (1998).

13. Repp, J., Meyer, G., Olsson, F. E. & Persson, M. Controlling the charge state of individual gold adatoms. *Science* **305**, 493–495 (2004).
14. Gross, L. *et al*. Scattering of surface state electrons at large organic molecules. *Phys. Rev. Lett.* **93**, 056103 (2004).
15. Auwärter, W. *et al*. A surface-anchored molecular four-level conductance switch based on single proton transfer. *Nat. Nanotechnol.* **7**, 41–46 (2012).
16. Crommie, M. F., Lutz, C. P. & Eigler, D. M. Imaging standing waves in a 2-dimensional electron-gas. *Nature* **363**, 524–527 (1993).
17. Li, J., Schneider, W.-D., Berndt, R. & Crampin, S. Electron confinement to nanoscale Ag islands on Ag(111): A quantitative study. *Phys. Rev. Lett.* **80**, 3332–3335 (1998).
18. Manoharan, H. C., Lutz, C. P. & Eigler, D. M. Quantum mirages formed by coherent projection of electronic structure. *Nature* **403**, 512–515 (2000).
19. Pennec, Y. *et al*. Supramolecular gratings for tuneable confinement of electrons on metal surfaces. *Nat. Nanotechnol.* **2**, 99–103 (2007).
20. Schiffrin, A. *et al*. Self-aligning atomic strings in surface-supported biomolecular gratings. *Phys. Rev. B* **78**, 035424 (2008).
21. Moon, C. R., M, L. S., Foster, B. K., Zeltzer, G. & Manoharan, H. C. Quantum holographic encoding in a two-dimensional electron gas. *Nat. Nanotechnol.* **4**, 167–172 (2009).
22. Klappenberger, F. *et al*. Dichotomous array of chiral quantum corrals by a self-assembled nanoporous kagomé network. *Nano Lett.* **9**, 3509–3514 (2009).
23. Klappenberger, F. *et al*. Tunable quantum dot arrays formed from self-assembled metal-organic networks. *Phys. Rev. Lett.* **106**, 026802 (2011).
24. Lobo-Checa, J. *et al*. Band formation from coupled quantum dots formed by a nanoporous network on a copper surface. *Science* **325**, 300–303 (2009).
25. Reinert, F., Nicolay, G., Schmidt, S., Ehm, D. & Hüfner, S. Direct measurements of the *L*-gap surface states on the (111) face of noble metals by photoelectron spectroscopy. *Phys. Rev. B* **63**, 115415 (2001).
26. Mugarza, A. & Ortega, J. E. Electronic states at vicinal surfaces. *J. Phys.: Condens. Matter* **15**, S3281 (2003).
27. Selloni, A., Carnevali, P., Tosatti, E. & Chen, C. D. Voltage-dependent scanning-tunneling microscopy of a crystal surface: Graphite. *Phys. Rev. B* **31**, 2602–2605 (1985).
28. Lang, N. D. Spectroscopy of single atoms in the scanning tunneling microscope. *Phys. Rev. B* **34**, 5947–5950 (1986).
29. Hörmandinger, G. Imaging of the Cu(111) surface state in scanning tunneling microscopy. *Phys. Rev. B* **49**, 13897–13905 (1994).
30. Kubby, J. A. & Boland, J. J. Scanning tunneling microscopy of semiconductor surfaces. *Surf. Sci. Rep.* **26**, 61–204 (1996).
31. Kliewer, J., Berndt, R. & Crampin, S. Scanning tunnelling spectroscopy of electron resonators. *New J. Phys.* **3**, 22 (2001).
32. Koslowski, B., Dietrich, C., Tschetschetkin, A. & Ziemann, P. Evaluation of scanning tunneling spectroscopy data: Approaching a quantitative determination of the electronic density of states. *Phys. Rev. B* **75**, 035421 (2007).
33. Wagner, C., Franke, R. & Fritz, T. Evaluation of I(V) curves in scanning tunneling spectroscopy of organic nanolayers. *Phys. Rev. B* **75**, 235432 (2007).
34. Ziegler, M., Néel, N., Sperl, A., Kröger, J. & Berndt, R. Local density of states from constant-current tunneling spectra. *Phys. Rev. B* **80**, 125402 (2009).
35. Passoni, M., Donati, F., Li Bassi, A., Casari, C. S. & Bottani, C. E. Recovery of local density of states using scanning tunneling spectroscopy. *Phys. Rev. B* **79**, 045404 (2009).
36. Li, J. T., Schneider, W. D. & Berndt, R. Local density of states from spectroscopic scanning-tunneling-microscope images: Ag(111). *Phys. Rev. B* **56**, 7656–7659 (1997).
37. Simmons, J. G. Electric tunnel effect between dissimilar electrodes separated by a thin insulating film. *J. Appl. Phys.* **34**, 2581–2590 (1963).
38. Wahl, P., Diekhöner, L., Schneider, M. A. & Kern, K. Background removal in scanning tunneling spectroscopy of single atoms and molecules on metal surfaces. *Rev. Sci. Inst.* **79**, 043104 (2008).
39. Bürgi, L., Jeandupeux, O., Hirstein, A., Brune, H. & Kern, K. Confinement of surface state electrons in fabry-pérot resonators. *Phys. Rev. Lett.* **81**, 5370–5373 (1998).
40. Stroscio, J. A., Feenstra, R. M. & Fein, A. P. Electronic structure of the Si(111) 2×1 surface by scanning-tunneling microscopy. *Phys. Rev. Lett.* **57**, 2579–2582 (1986).
41. Kühne, D. *et al*. Self-assembly of nanoporous chiral networks with varying symmetry from sexiphenyl-dicarbonitrile on Ag(111). *J. Phys. Chem. C* **113**, 17851–17859 (2009).
42. Sautet, P. Images of adsorbates with the scanning tunneling microscope: Theoretical approaches to the contrast mechanism. *Chem. Rev.* **97**, 1097–1116 (1997).
43. Weber-Bargioni, A. *et al*. Visualizing the frontier orbitals of a conformationally adapted metalloporphyrin. *ChemPhysChem* **9**, 89–94 (2008).
44. Auwärter, W. *et al*. Site-specific electronic and geometric interface structure of Co-tetraphenyl-porphyrin layers on Ag(111). *Phys. Rev. B* **81**, 245403 (2010).
45. Vitali, L. *et al*. Portrait of the potential barrier at metal-organic nanocontacts. *Nat. Mater.* **9**, 320–323 (2010).
46. Boulanger-Lewandowski, N. & Rochefort, A. Intrusive STM imaging. *Phys. Rev. B* **83**, 115430 (2011).
47. Gross, L. *et al*. High-Resolution Molecular Orbital Imaging Using a p-Wave STM Tip. *Phys. Rev. Lett.* **107**, 086101 (2011).
48. France, C. B. & Parkinson, B. A. Physical and electronic structure of p-sexiphenyl on Au(111). *Appl. Phys. Lett.* **82**, 1194–1196 (2003).
49. Clair, S. *Investigation of Low-Dimensional Supramolecular Architectures by Low-Temperature Scanning Tunneling Microscopy.* Ph. D. thesis, Ecole Polytechnique Federale de Lausanne (2004).
50. Clair, S. *et al*. STM study of terephthalic acid self-assembly on Au(111): Hydrogen-bonded sheets on an inhomogeneous substrate. *J. Phys. Chem. B* **108**, 14585–14590 (2004).

Acknowledgments

The authors would like to thank C.A. Palma for proofreading the manuscript and helpful discussions. Funding by the German Research Foundation (DFG) (*via* BA 3395/2-1, the TUM International Graduate School of Science and Engineering (IGSSE) and the TUM Institute of Advanced Study (IAS)) and the European Union (*via* ERC Advanced Grant MolArt (°247299)) is gratefully acknowledged.

Author contributions

W.K., D.K. and F.K. carried out the experiments. W.K. F.K. and J.V.B. wrote the manuscript. F.K. and J.V.B. conceived the experiments and guided the research.

Additional information

Supplementary information accompanies this paper at http://www.nature.com/scientificreports

Competing financial interests: The authors declare no competing financial interests.

How to cite this article: Krenner, W., Kühne, D., Klappenberger, F. & Barth, J.V. Assessment of Scanning Tunneling Spectroscopy Modes Inspecting Electron Confinement in Surface-Confined Supramolecular Networks. *Sci. Rep.* **3**, 1454; DOI:10.1038/srep01454 (2013).

SCIENTIFIC REPORTS

DOI: 10.1038/srep03772

SUBJECT AREAS:
ELECTRONIC PROPERTIES AND MATERIALS
SURFACES, INTERFACES AND THIN FILMS
MOLECULAR SELF-ASSEMBLY
IMAGING TECHNIQUES

SCIENTIFIC REPORTS:
3 : 1454
DOI: 10.1038/srep01454
(2013)

Published:
18 March 2013

Updated:
23 January 2014

CORRIGENDUM: Assessment of Scanning Tunneling Spectroscopy Modes Inspecting Electron Confinement in Surface-Confined Supramolecular Networks

Wolfgang Krenner, Dirk Kühne, Florian Klappenberger & Johannes V. Barth

This Article contains errors in Equations (1) and (3). In these equations "eV" should read "eV$_B$", and in Equation (1) "(eV-E)" should read "(E-eV$_B$)".

Equation (1) should read:

$$I_T \propto \int_0^{eV_B} \rho_T(E-eV_B)\rho_S(\vec{r}_T,E)\,T(z,\,eV_B,\,E)\mathrm{d}E$$

Equation (3) should read:

$$\left.\frac{\mathrm{d}I}{\mathrm{d}V}\right|_{V_B} \propto \rho_S(eV_B)T(z,eV_B) + \int_0^{eV_B} \rho_S(E)\frac{\partial T(eV_B,\,E)}{\partial V}\mathrm{d}E.$$